Journal of Medical Imaging

MedicalImaging.SPIEDigitalLibrary.org

Semiautomated biventricular segmentation in three-dimensional echocardiography by coupled deformable surfaces

Jørn Bersvendsen
Fredrik Orderud
Øyvind Lie
Richard John Massey
Kristian Fosså
Raúl San José Estépar
Stig Urheim
Eigil Samset

SPIE.

Jørn Bersvendsen, Fredrik Orderud, Øyvind Lie, Richard John Massey, Kristian Fosså, Raúl San José Estépar, Stig Urheim, Eigil Samset, "Semiautomated biventricular segmentation in three-dimensional echocardiography by coupled deformable surfaces," *J. Med. Imag.* **4**(2), 024005 (2017), doi: 10.1117/1.JMI.4.2.024005.

Journal of Medical Imaging 4(2), 024005 (Apr–Jun 2017)

Semiautomated biventricular segmentation in three-dimensional echocardiography by coupled deformable surfaces

Jørn Bersvendsen,[a,b,c,*] Fredrik Orderud,[b] Øyvind Lie,[c,d] Richard John Massey,[d] Kristian Fosså,[e] Raúl San José Estépar,[f] Stig Urheim,[d,g] and Eigil Samset[a,b,c]
[a]GE Vingmed Ultrasound AS, Horten, Norway
[b]University of Oslo, Department of Informatics, Oslo, Norway
[c]Center for Cardiological Innovation, Oslo, Norway
[d]Oslo University Hospital, Department of Cardiology, Oslo, Norway
[e]Oslo University Hospital, Department of Radiology and Nuclear Medicine, Oslo, Norway
[f]Brigham and Women's Hospital, Harvard Medical School, Boston, Massachusetts, United States
[g]Oslo University Hospital, Institute for Surgical Research, Oslo, Norway

Abstract. With the advancement of three-dimensional (3-D) real-time echocardiography in recent years, automatic creation of patient specific geometric models is becoming feasible and important in clinical decision making. However, the vast majority of echocardiographic segmentation methods presented in the literature focus on the left ventricle (LV) endocardial border, leaving segmentation of the right ventricle (RV) a largely unexplored problem, despite the increasing recognition of the RV's role in cardiovascular disease. We present a method for coupled segmentation of the endo- and epicardial borders of both the LV and RV in 3-D ultrasound images. To solve the segmentation problem, we propose an extension of a successful state-estimation segmentation framework with a geometrical representation of coupled surfaces, as well as the introduction of myocardial incompressibility to regularize the segmentation. The method was validated against manual measurements and segmentations in images of 16 patients. Mean absolute distances of 2.8 ± 0.4 mm, 3.2 ± 0.7 mm, and 3.1 ± 0.5 mm between the proposed and reference segmentations were observed for the LV endocardium, RV endocardium, and LV epicardium surfaces, respectively. The method was computationally efficient, with a computation time of 2.1 ± 0.4 s. [DOI: 10.1117/1.JMI.4.2.024005]

Keywords: medical imaging; image segmentation; three-dimensional echocardiography; surface representation.

Paper 16019RRR received Jan. 27, 2016; accepted for publication May 1, 2017; published online May 24, 2017.

1 Introduction

Evaluation of the heart's structure and function is vital for the diagnosis and treatment of cardiovascular diseases.

For this purpose, three-dimensional real-time echocardiography (3DRTE) has been making its way into clinical use in recent years.[1] Compared to conventional two-dimensional (2-D) echocardiography, 3DRTE allows a more complete and accurate appreciation of the heart's complex 3-D structure and motion. However, because of the large increase in information and complexity in these 3-D images, clinicians must rely on computer-aided methods for their clinical quantification and decision making. Of particular interest is the extraction of patient-specific geometric models of heart structures. Such models have many uses, including quantification of cardiac chamber shape, size, and function, as well surgical planning.

In this paper, we present a method for coupled segmentation of the endo- and epicardial borders of both the left ventricle (LV) and right ventricle (RV) in 3DRTE images. Although the vast majority of 3DRTE segmentation methods presented in the literature focus on the LV endocardial border, segmentation of the other cardiac chambers are necessary to assess a wider range of cardiac diseases and procedures. Furthermore, as the chambers interact in performing the pumping function, multichamber models could allow a more complete evaluation of the clinical condition. Finally, segmentation of the epicardium (EPI) allows the measurement of the myocardial mass, which is a well-established measurement and an independent risk factor for cardiovascular events.[2]

Segmentation of the LV in 3-D ultrasound images is commonly solved by sequential fitting of an endocardial surface representation to the image. Many different representations have been proposed, including explicit surfaces such as spline and subdivision surfaces and implicit surfaces such as a level-set of higher-dimension functions. The fitting algorithm is commonly an energy minimization formulation or an optimization of boundary edge criteria. It is typically necessary to introduce prior shape information and regularization in the fitting process to overcome noise, artifacts, and missing edges in the ultrasound images.

Epicardial segmentation has received less attention in the literature and is generally more challenging than endocardial segmentation. For instance, the contrast between the ventricle blood pool and myocardium is typically much higher than the contrast between the myocardium and surrounding tissues, making the

*Address all correspondence to: Jørn Bersvendsen, E-mail: jorn.bersvendsen@gmail.com

2329-4302/2017/$25.00 © 2017 SPIE

epicardial border harder to detect.[3] To solve this problem, Orderud et al.[4] extended a deformable surface segmentation method for the LV,[5] using separate endocardial end epicardial surfaces sharing a global pose transform. In another study, Myronenko et al.[6] presented a method for LV endo- and epicardial border tracking based on a combination of image texture and gradient information.

Because of the high water content, the myocardium is believed to be nearly incompressible. This means that the myocardial volume remains roughly unchanged during the cardiac cycle, with changes of less than 5%.[3,7,8] The incompressibility has been used to improve segmentation results of 3DRTE[3] and MRI.[9] Zhu et al.[3] used speckle statistics together with the myocardial incompressibility constraint to evolve separate LV endo- and epicardial surfaces from an initial segmentation. A significant accuracy improvement was discovered with the introduction of the incompressibility constraint, compared to both a similar thickness constraint and an unconstrained segmentation.

The field of RV segmentation in 3DRTE images is less mature compared to the LV. The LV methods are typically not immediately applicable to the RV, as the RV has a more complex shape and larger interpatient variation. Furthermore, the RV endocardium (RV-END) is typically harder to define by ultrasound because of trabeculations and missing edges due to its position relative to the lung and sternum. Angelini et al.[10] applied a level-set framework to separately segment both the LV and RV endocardial borders. Recently, Stebbing et al.[11] proposed an RV segmentation method where the endocardial surface is represented by a Loop subdivision surface and fitted by energy minimizing across multiple views of the same patient, or across multiple patients. Finally, we previously presented a method for RV segmentation based on a statistical shape model and Kalman filter state estimation.[12]

The method presented in this paper allows a coupled segmentation of endo- and epicardial borders of the LV and RV. The endo- and epicardial surfaces are represented as coupled deformable surfaces and fitted to the image using a real-time segmentation framework previously applied to the LV[5] and RV[12] separately. Incompressibility of the myocardium is introduced by regularizing the myocardial volume during the cardiac cycle. The method is used to measure chamber volumes and ejection fractions (EFs), as well as the LV myocardial mass. To evaluate the method, the semiautomated results were compared with manual segmentations in 3DRTE, as well as volume measurements in MRI, in images of 16 patients.

2 Biventricular Surface Representation

In this section, we present a surface representation for coupled basis surfaces defined by a common control mesh and local thicknesses. Although the method discussed here generalizes to 2-D splines, we will focus on 3-D surfaces.

2.1 *Coupled Surfaces*

Given a control mesh with N_v vertices

$$\mathbf{Q} = [\mathbf{q}_1, \mathbf{q}_2, \ldots, \mathbf{q}_{N_v}], \tag{1}$$

and topology $\mathcal{T}$, a family of surface representations exist that generates points $\mathbf{p}$ on a smooth surface defined by the function $\mathbf{p}(\mathbf{u}) : \Omega_u \mapsto \mathbb{R}^3$ on the form

$$\mathbf{p}(\mathbf{u}) = \sum_{i=1}^{N_v} b_i(\mathbf{u}, \mathcal{T})\mathbf{q}_i, \tag{2}$$

where Ω_u is the surface domain, i.e., $\Omega_u \subset \mathbb{R}^2$ for 3-D basis surfaces, and $\mathbf{u} \in \Omega_u$ is a surface coordinate. Examples of such surfaces include Doo–Sabin,[5,13] Catmull–Clark,[14,15] and Loop[16,17] subdivision surfaces. These surfaces can be split into several patches, where each patch $\mathcal{P}$ has region of support $\Omega_\mathcal{P}$, such that the local surface is given by

$$\mathbf{p}_\mathcal{P}(\mathbf{u}) = \sum_{i \in \Omega_\mathcal{P}} b_i(\mathbf{u})\mathbf{q}_i \quad \forall\, \mathbf{u} \in [0,1] \times [0,1]. \tag{3}$$

Figure 1 shows a patch with its control mesh and resulting surface.

2.1.1 *Thickness*

In the general case, let there be N_s surfaces defined on the control mesh $\mathbf{Q}$ where each surface $\mathcal{S}_i$ is a collection of patches centered on a subset $\Omega_{\mathcal{S}_i} \subset [1, 2, \ldots, N_v]$ of the control vertices, i.e.,

$$\mathcal{S}_i = \{\mathcal{P}_{i,j} : j \in \Omega_{\mathcal{S}_i}\}, \tag{4}$$

where $\mathcal{P}_{i,j}$ is the patch of the i'th surface centered on the j'th control vertex. Figure 2(a) shows a simplified illustration of three surfaces defined on a control mesh of four vertices.

Each patch $\mathcal{P}_{i,j}$ is associated with a thickness $t_{i,j}$. To create a thick model, the control vertices are displaced separately for each surface. The locally deformed control vertices $\tilde{\mathbf{Q}}_i$ of surface $\mathcal{S}_i$

$$\tilde{\mathbf{Q}}_i(\mathbf{t}_i) = [\tilde{\mathbf{q}}_{i,1}, \tilde{\mathbf{q}}_{i,2}, \ldots, \tilde{\mathbf{q}}_{i,N_v}], \tag{5}$$

are calculated by

$$\tilde{\mathbf{q}}_{i,k} = \begin{cases} \mathbf{q}_k + \mathbf{n}_{i,j} t_{i,j}, & \text{if } k \in \Omega_{\mathcal{S}_i} \\ \mathbf{q}_k, & \text{otherwise} \end{cases}, \tag{6}$$

where $\mathbf{n}_{i,j}$ is the normal direction at the center of patch $\mathcal{P}_{i,j}$ and $\mathbf{t}_i = \{t_{i,j}\}$ is the vector of patch thicknesses. Figure 2(b) shows the local displacement of three surfaces sharing a central vertex.

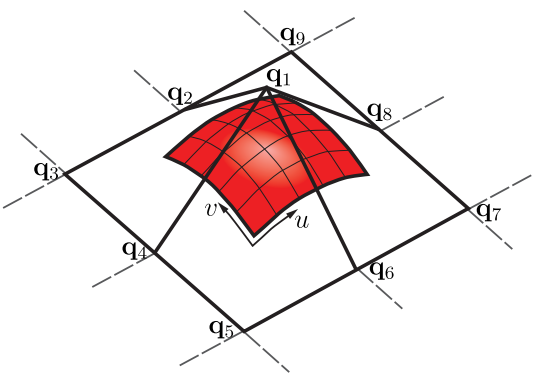

Fig. 1 Illustration of a basis surface patch $\mathbf{p}(u, v)$ controlled by a control mesh $\mathbf{Q} = [\mathbf{q}_1, \mathbf{q}_2, \ldots, \mathbf{q}_9]$ centered on $\mathbf{q}_1$.

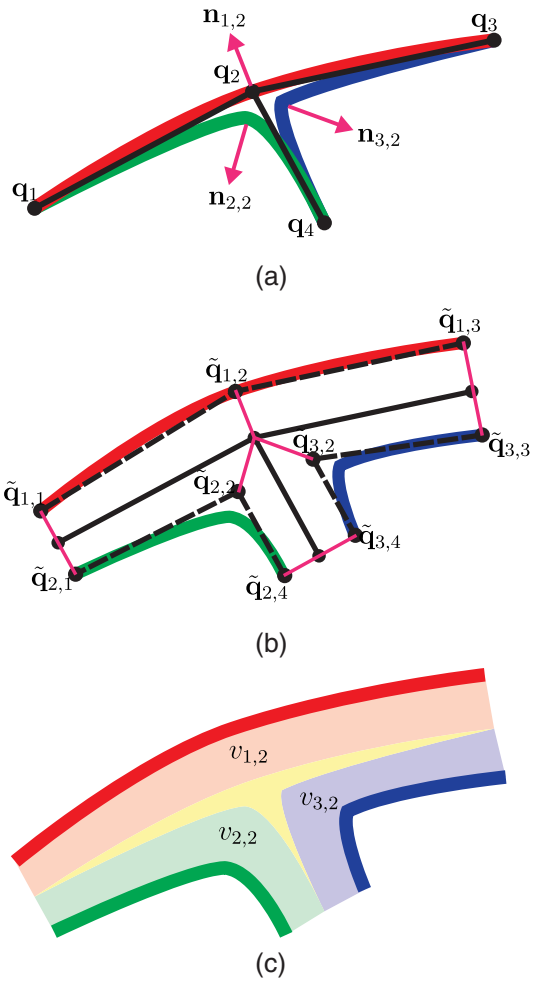

Fig. 2 Illustration of the creation of a thick model from a shared midwall control mesh. In this case, three surface patches share a single central vertex $\mathbf{q}_2$. (a) Control mesh and initial surface patches. (b) Local thickness deformations of the control mesh and resulting displaced surfaces. (c) Resulting thick model.

2.2 *Model Parameterization*

2.2.1 *Midwall control mesh*

Following the approach described in Sec. 2.1, we use three Doo–Sabin subdivision surfaces to represent the LV endocardium (LV-END), RV-END, and EPI borders. All surfaces share the same underlying midwall control mesh with 54 vertices

$$\mathbf{Q} = [\mathbf{q}_1, \mathbf{q}_2, \ldots, \mathbf{q}_{54}]. \tag{7}$$

Figure 3 shows the midwall control mesh used to represent the biventricular model and the corresponding LV, RV, and EPI surfaces.

Each vertex $\mathbf{q}_i$ of the midwall control mesh has a single degree of freedom $x_{d,i}$ specifying the deformation along a single axis $\mathbf{d}_i$ such that

$$\mathbf{q}_i = \mathbf{q}_{i,0} + \mathbf{d}_i x_{d,i}, \tag{8}$$

where $\mathbf{q}_{i,0}$ is the corresponding initial control point. The deformation directions are the initial normal directions of the EPI surface.

For each of the three surfaces $\mathcal{S}_i$, we apply a thickness $t_{i,j}$ along the initial surface normals $\mathbf{n}_{i,j}$ such that the resulting control mesh $\tilde{\mathbf{Q}}_i = [\tilde{\mathbf{q}}_{i,1}, \tilde{\mathbf{q}}_{i,2}, \ldots, \tilde{\mathbf{q}}_{i,54}]$ is given by

$$\tilde{\mathbf{q}}_{i,j} = \mathbf{q}_j + \mathbf{n}_{i,j} t_{i,j}, \tag{9}$$

and the resulting surface is given by

$$\tilde{\mathbf{p}}_i(u, v, \mathbf{x}_d, \mathbf{t}_i) = \sum_{j=1}^{54} b_{i,j}(u, v) \tilde{\mathbf{q}}_{i,j}, \tag{10}$$

where $b_{i,j}(u, v)$ are the Doo–Sabin basis functions at a surface location (u, v) and $\mathbf{x}_d$ and $\mathbf{t}_i$ are the midwall deformation and thickness states, respectively.

2.2.2 *Patch volumes*

When the ventricles contract and shorten during the cardiac cycle, the myocardium thickens as the myocardial volume remains approximately constant. To model this in a natural way, we move from the thickness parameterization described in Eq. (9) to a volume parameterization. This makes it natural to use local patch volume regularization as a surrogate for myocardial mass conservation.

Using the divergence theorem, we can relate the patch thicknesses with the resulting volumes. This relationship can then be used to provide a model that is parameterized by local patch volumes. For each surface $\mathcal{S}_i$, volumes $v_{i,j}$ of all patches $\mathcal{P}_{i,j}$ are given by the midwall deformation states $\mathbf{x}_d$ and thickness states $\mathbf{t}_i = \{t_{i,j}\}$

$$v_{i,j} = v_{i,j}(\mathbf{x}_d, \mathbf{t}_i). \tag{11}$$

See the Appendix for details on deriving Eq. (11).

Let $\tilde{\mathbf{v}}_i = \{v_{i,j}\}$ be the vector of volumes of each patch in surface $\mathcal{S}_i$, with initial volumes $\tilde{\mathbf{v}}_{i,0} = \{v^0_{i,j}\}$. The volume–thickness relationship in Eq. (11) is simplified by approximating it with a linearization around the initial state

$$\tilde{\mathbf{v}}_i \approx \mathbf{A}_i(\mathbf{t}_i - \mathbf{t}_{i,0}) + \mathbf{C}_i(\mathbf{x}_d - \mathbf{x}_{d,0}) + \tilde{\mathbf{v}}_{i,0}, \tag{12}$$

where

$$\mathbf{A}_i = \left.\frac{\partial \mathbf{v}_i}{\partial \mathbf{t}_i}\right|_{\substack{\mathbf{t}_{i,0} \\ \mathbf{x}_{d,0}}}, \tag{13}$$

$$\mathbf{C}_i = \left.\frac{\partial \mathbf{v}_i}{\partial \mathbf{x}_d}\right|_{\substack{\mathbf{t}_{i,0} \\ \mathbf{x}_{d,0}}}. \tag{14}$$

2.2.3 *Scaling*

We introduce a global scaling state s, used to scale the model into the image, such that a point $\mathbf{p}$ on the scaled model is given by $\mathbf{p} = s\tilde{\mathbf{p}}$, where $\tilde{\mathbf{p}}$ is given by Eq. (10). The vector $\mathbf{v}^p_i$ of scaled patch volumes is then $\mathbf{v}^p_i = s^3\tilde{\mathbf{v}}_i$, where $\tilde{\mathbf{v}}_i$ is given by the approximation in Eq. (12).

2.2.4 *Control vertex volumes*

It is desirable to combine the patch volumes $\mathbf{v}^p_i$ to a single volume state v^n_i wherever two or more surfaces share the central control vertex. This reduces the number of states and ensures

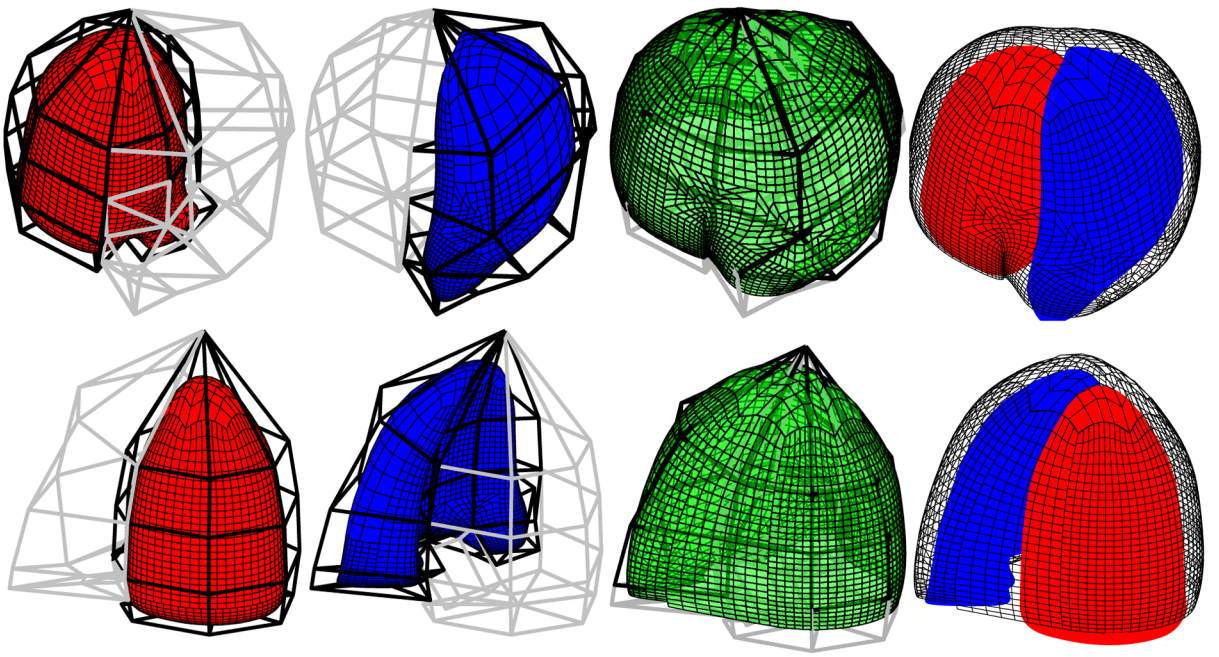

Fig. 3 Control mesh and resulting subdivision surfaces. The two rows show the same model from different sides. From the left: LV, RV, EPI, and all surfaces.

a stable distribution of volume for all surfaces, e.g., on both sides of the myocardium midwall. Let $\mathbf{v}^n = \{v_j^n\}$ be the vector of volumes for all control vertices

$$v_j^n = \sum_{k \in \Omega_k} v_{k,j}, \tag{15}$$

where Ω_k is the set of surfaces with patches centered on the k'th midwall vertex. The model is parameterized by volume changes $\mathbf{v}$ with respect to the initial volumes $\mathbf{v}_0^n$

$$\mathbf{v} = \mathbf{v}^n - \mathbf{v}_0^n. \tag{16}$$

The control vertex volumes are distributed on each surface in proportion to the initial volumes

$$v_{i,j} = v_j^n \frac{v_{i,j}^0}{\sum_{\Omega_k} v_{k,j}^0}, \tag{17}$$

such that

$$\mathbf{v}_i^p = \mathbf{P}_i \mathbf{v}^n. \tag{18}$$

The local surface thicknesses are then given by Eqs. (18) and (12), resulting in

$$\mathbf{t}_i = \mathbf{A}_i^{-1}\left[\mathbf{P}_i \tilde{\mathbf{v}}^n \frac{1}{s^3} - \mathbf{v}_{i,0}^p \left(\frac{s_0^3}{s^3} - 1\right)\right] - \mathbf{A}_i^{-1}\mathbf{C}_i(\mathbf{x} - \mathbf{x}_0) + \mathbf{t}_{i,0}. \tag{19}$$

The state Jacobians for the surface $\mathcal{S}_i$, required to solve the segmentation problem, are given by

$$\frac{\partial \mathbf{p}_i}{\partial s} = \mathbf{Q}\mathbf{b}_i - \frac{3}{s^3}\mathbf{N}_i\mathbf{B}_i\mathbf{A}_i^{-1}(\mathbf{P}_i\mathbf{v} - \mathbf{v}_{i,0}^p s_0^3), \tag{20}$$

$$\frac{\partial \mathbf{p}_i}{\partial \mathbf{x}_d} = s\mathbf{D}\mathbf{B}_i - s\mathbf{N}_i\mathbf{B}_i\mathbf{A}_i^{-1}\mathbf{C}_i, \tag{21}$$

$$\frac{\partial \mathbf{p}_i}{\partial \mathbf{v}} = \frac{1}{s^2}\mathbf{N}_i\mathbf{B}_i\mathbf{A}_i^{-1}\mathbf{C}_i, \tag{22}$$

where $\mathbf{b}_i$ is the vector of basis functions for $\mathcal{S}_i$ at $\mathbf{p}_i$, $\mathbf{B}_i = \mathrm{diag}(\mathbf{b}_i)$, $\mathbf{D}$ is a matrix of the midwall deformation directions, and $\mathbf{N}_i$ is a matrix of the thickness normal directions for $\mathcal{S}_i$.

2.2.5 *Pose transform*

To place the model within the image, we introduce a pose transform $\mathbf{p}_{\mathrm{image}} = \mathbf{T}(\mathbf{p}_i, \mathbf{x}_p)$ allowing for translation and rotation. The combined state vector is $\mathbf{x} = [\mathbf{x}_p, s, \mathbf{x}_d, \mathbf{v}]$, where $\mathbf{x}_p$ is the pose transform states with six degrees of freedom. The combined Jacobian is given by

$$\frac{\partial \mathbf{p}_{\mathrm{image}}}{\mathbf{x}} = \left[\frac{\partial \mathbf{T}}{\partial \mathbf{x}_p}, \frac{\partial \mathbf{T}}{\partial \mathbf{p}_i}\frac{\partial \mathbf{p}_i}{\partial s}, \frac{\partial \mathbf{T}}{\partial \mathbf{p}_i}\frac{\partial \mathbf{p}_i}{\partial \mathbf{x}_d}, \frac{\partial \mathbf{T}}{\partial \mathbf{p}_i}\frac{\partial \mathbf{p}_i}{\partial \mathbf{v}}\right]. \tag{23}$$

3 Segmentation

The method presented here is an application of a real-time volumetric segmentation framework previously applied on the LV,[4,5,18] RV,[12] and aortic root.[19] For a detailed description of the framework, the reader is referred to previous works.[5,12]

3.1 *Initialization*

Before performing the state estimation, the model is initialized by manually identifying the following eight anatomical landmarks in end diastole: mitral valve (MV) center, tricuspid valve (TV) center, aortic valve (AV) center, LV apex, anterior and

posterior LV–RV junction points, and a single point on the lateral RV free wall.

Because the parameterization presented in Sec. 2.2.1 only allows the control mesh to deform in the normal direction, the model lacks the necessary degrees of freedom to capture differences in RV width/height ratios and LV outflow tract (LVOT) directions. To mitigate this, the midwall control mesh is personalized by adjusting the distance between LV–RV junction points, LVOT direction, and RV diameter, based on the manually identified landmarks prior to segmentation. The initial pose and scale parameters are then calculated by rigidly registering the model to the landmarks.

3.2 *Kalman Filter Process*

The segmentation is represented as a state estimation problem and solved with an extended Kalman filter. Iteratively for each frame in the cycle, the following processing chain is performed:

1. The next state is predicted as a combination of the previous state estimate $\hat{\mathbf{x}}_{k-1|k-1}$, with associated covariance matrix $\hat{\mathbf{P}}_{k-1|k-1}$ and a motion model $\tilde{\mathbf{x}}_k$ by

$$\hat{\mathbf{x}}_{k|k-1} = \mathbf{A}\hat{\mathbf{x}}_{k-1|k-1} + (\mathbf{I} - \mathbf{A})\tilde{\mathbf{x}}_k, \tag{24}$$

$$\hat{\mathbf{P}}_{k|k-1} = \mathbf{A}\hat{\mathbf{P}}_{k-1|k-1}\mathbf{A}^\top + \mathbf{Q}_k, \tag{25}$$

   where $\mathbf{A}$ is a diagonal matrix specifying the regularization strength for each state and $\mathbf{Q}_k$ is the estimated prediction noise. $\mathbf{A}$ and $\mathbf{Q}_k$ are used to control the regularization behavior of the motion model and are set prior to segmentation.

   The motion model $\tilde{\mathbf{x}}_k$ starts from the initialization and follows a predefined contraction pattern. The pattern includes longitudinal and radial shortening of both ventricles, while the myocardial volume states are predicted to remain unchanged. This simple motion model increases the accuracy of the prediction and, hence, the location of the edge detection samples in the next step.

2. Edge detection is performed normal to the predicted endo- and epicardial surfaces at 2200 evenly distributed points. For each edge point, a displacement v_i with estimated variance r_i is detected by searching along the normal vector $\mathbf{n}_i$ using the least mean squares fit to an intensity step profile. Outlier edges are rejected based on the intensity step height and differences between neighboring edges.

3. The previous estimate, prediction, and edge measurements are fused by

$$\mathbf{h}_i^\top = \mathbf{n}_i^\top \mathbf{J}_i, \tag{26}$$

$$\mathbf{P}_{k|k}^{-1} = \mathbf{P}_{k|k-1}^{-1} + \sum_i \mathbf{h}_i r_i^{-1} \mathbf{h}_i^\top, \tag{27}$$

$$\hat{\mathbf{x}}_{k|k} = \hat{\mathbf{x}}_{k|k-1} + \mathbf{P}_{k|k} \sum_i \mathbf{h}_i r_i^{-1} v_i, \tag{28}$$

   where v_i, r_i, $\mathbf{n}_i$, and $\mathbf{J}_i$ are the edge displacement, measurement variance, normal vector, and state Jacobian matrix, respectively.

The parameters that substantially influence the Kalman filter segmentation are the initial state covariance estimate ($\mathbf{P}_0$), estimated noise values for the process and edge measurements ($\mathbf{Q}_k$ and r_i, respectively), and the regularization in the prediction step ($\mathbf{A}$).

To prevent the segmentation from lagging behind the image and to enforce a cyclic segmentation, a Kalman smoother[20] approach is applied. The process is repeated starting from the last frame and iterating backward in time, and the final state estimate $\hat{\mathbf{x}}$ is fused by

$$\mathbf{P}_k = (\mathbf{P}_{f,k}^{-1} + \mathbf{P}_{b,k}^{-1})^{-1}, \tag{29}$$

$$\hat{\mathbf{x}}_k = \mathbf{P}_k(\mathbf{P}_{f,k}^{-1}\hat{\mathbf{x}}_{f,k} + \mathbf{P}_{b,k}^{-1}\hat{\mathbf{x}}_{b,k}), \tag{30}$$

where $\hat{\mathbf{x}}_f$, $\mathbf{P}_f$ and $\hat{\mathbf{x}}_b$, $\mathbf{P}_b$ are the forward and backward iteration estimates, respectively.

3.3 *Dual-Pass State Estimation*

We apply the whole Kalman filter process in two passes; first to identify the pose transform and myocardial volume, then to optimize the local shape deformations. This allows the patch volumes to converge before applying volume regularization.

In the first pass, the local shape deformation process noise is set fairly low compared to the other states, resulting in a stiff model while allowing for rapid changes in global pose and patch volumes.

In the second pass, the global pose transform of the first pass is used as prediction states within the Kalman filter. Similarly, the predicted volume is set to the average patch volumes of the first pass with low process noise and high regularization, effectively performing weighted volume conservation.

4 Validation

The segmentation was validated on retrospective 3DRTE recordings of 16 patients with aortic insufficiency. This is a subset of the data used in a previous validation of an RV segmentation method.[12] The patient characteristics are given in Table 1. Segmentation quality was evaluated by calculating the Dice's coefficient (DICE) and the surface errors mean absolute distance (MAD), mean signed distance (MSD), and Hausdorff distance (HD) with respect to manual segmentation. In addition, the clinical indices end diastolic volume (EDV), end systolic volume (ESV), Stroke volume (SV), and EF were compared to manual measurements in MRI and 3DRTE.

Table 1 Patient characteristics of the 16 images used for validation.

Age, year	48 ± 15
Male, *n*	14 (88%)
Weight, kg	79 ± 9
Height, cm	177 ± 9
LV hypertension, *n*	1 (6%)
LV hypertrophy, *n*	10 (67%)

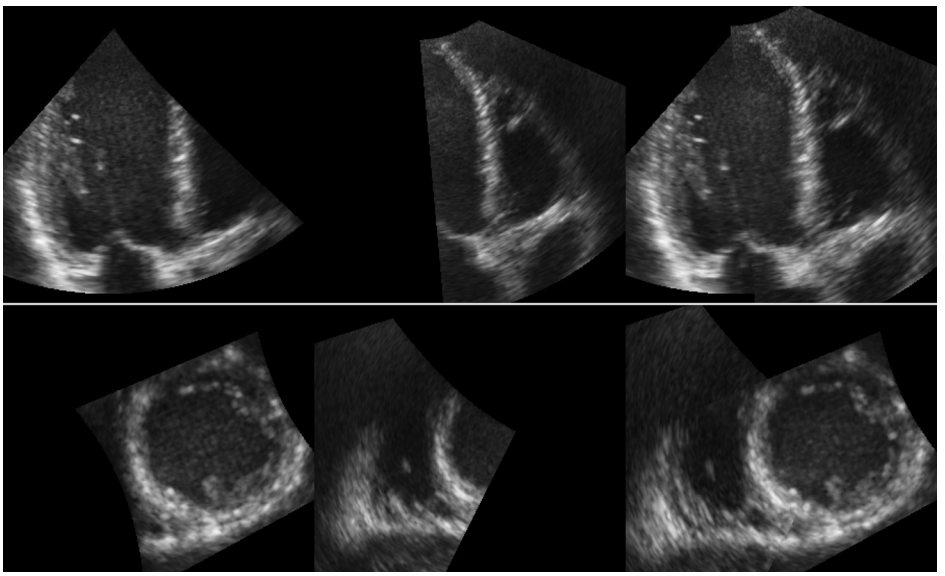

Fig. 4 Example result of image fusion between LV and RV.

4.1 *3DTTE*

4.1.1 *Acquisition*

For each patient, two separate 3DTTE recordings were acquired from an apical position. The probe was moved slightly between the acquisitions to individually capture both ventricles as best as possible. The images were recorded using ECG-gated multibeat acquisitions under a breath-hold. All images were acquired on a Vivid E9 scanner using a 4V probe (GE Vingmed Ultrasound AS, Horten, Norway).

4.1.2 *Fusion*

For each patient, the LV and RV images were spatio-temporally registered together by aligning the following manually annotated

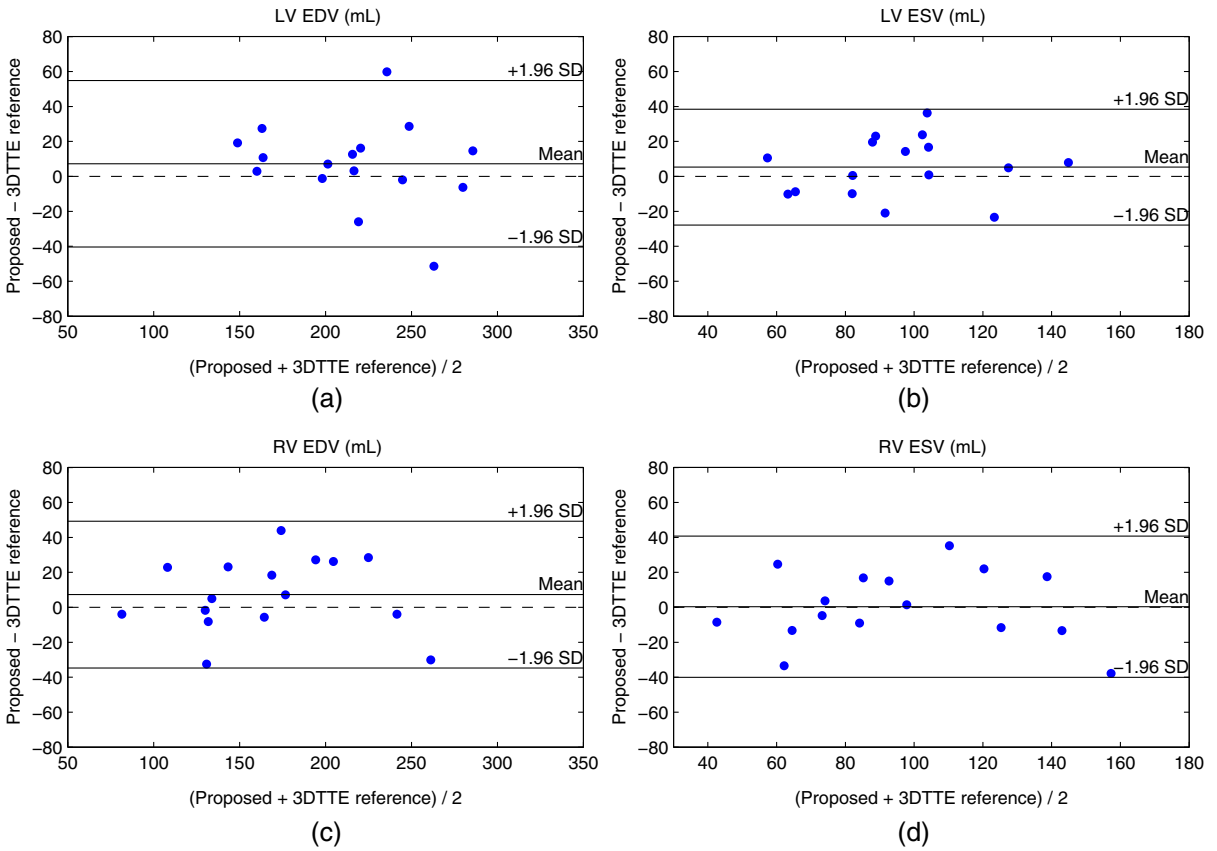

Fig. 5 Comparison of (a), (c) end-diastolic and (b), (d) end-systolic volumes of the (a), (b) left and (c), (d) right ventricles, as measured by the proposed method, with respect to manual measurements in 3DTTE.

Table 2 Results of surface-metric validation.

	Fused images		LV image only		RV image only	
	EPI	LV-END	RV-END	EPI	LV-END	RV-END
Mean AD	3.1 ± 0.5	2.8 ± 0.4	3.2 ± 0.7	3.0 ± 0.5	2.8 ± 0.4	3.0 ± 0.6
Median AD	2.6 ± ±0.4	2.5 ± 0.4	2.5 ± 0.5	2.5 ± 0.3	2.6 ± 0.4	2.5 ± 0.4
Mean SD	0.4 ± 1.0	0.2 ± 0.9	−0.6 ± 0.9	0.3 ± 0.9	0.2 ± 0.9	−0.3 ± 0.8
Median SD	0.5 ± 1.3	0.7 ± 1.1	−0.3 ± 1.2	0.5 ± 1.2	0.7 ± 1.1	−0.1 ± 1.2
Hausdorff distance	10.3 ± 2.5	8.8 ± 3.1	14.0 ± 5.5	10.0 ± 2.3	9.0 ± 2.5	13.6 ± 5.2

Note: All values are mean ± SD (mm).
AD, absolute distance; SD, signed distance; LV, left ventricle; RV, right ventricle; EPI, epicardial; END, endocardial.

landmarks: MV center, AV center, TV center, and LV apex and the following valvular events: MV closing, AV opening, AV closing, and MV opening. The sequences were temporally aligned by piecewise linear interpolation of the valve event times and spatially aligned by rigid procrustes alignment with unity scaling. Translation and rotation were manually adjusted after landmark registration to get a proper fusion. Figure 4 shows an example of LV–RV fusion.

4.1.3 *Reference segmentation*

Reference surfaces and clinical indices were acquired using the 4D AutoLVQ software (GE Vingmed Ultrasound, Horten, Norway) and 4D RV-Function software (TomTec Imaging Systems, Munich, Germany) for the LV and RV, respectively. In both tools, the proposed contours were manually adjusted to best match the endocardial borders by an experienced cardiologist.

4.1.4 *Automated segmentation*

The following landmarks were identified in the fused LV + RV image using a dedicated software: LV apex, MV, AV, and TV valve centers, anterior and posterior LV–RV junction points, and lateral RV free wall. The proposed automated segmentation method was then run on the image without any further manual involvement. To assess if the biventricular model could function as a standalone LV or RV segmentation, this procedure was done for the LV and RV images independently, as well as for the fused image. To assess the interobserver variability of the clinical measurements done by the automated method, the landmarks were annotated by a second observer.

4.1.5 *Surface error indices*

The surface error metrics were evaluated separately for the three surfaces LV-END, RV-END, and EPI and across all frames for each image. The 4D AutoLVQ software used to generate the LV-EPI reference produces a single ellipsoid surface partially covering the LV free wall EPI and the RV septal END. The EPI surface errors were, therefore, calculated between the reference LV-EPI surface and the proposed EPI and septal part of RV-END.

4.2 *MRI*

MRI images were acquired with Siemens 1.5 T scanners (Siemens Avanto and Siemens Sonata; Siemens Medical Systems, Erlangen, Germany) as previously described,[12] using a breath-hold, prospectively ECG-triggered, segmented, balanced-steady-state free precession gradient-echo cine sequence with minimum echo and repetition times. Slices were 6-mm thick with a 4-mm short-axis interslice gap, a spatial resolution of 1.9 × 1.3 mm, and a temporal resolution of 30 to 35 ms. Endocardial borders were traced manually at a picture archiving and communication system (PACS) workstation (Sectra Medical Systems AB, Linköping, Sweden). RV and RV volumes and EFs were calculated by short-axis slice summation.

5 Results

All 16 cases were successfully segmented with a computation time 2.1 ± 0.4 s (60 ± 1 ms per frame). Segmentation of the fused LV + RV image resulted in MAD and MSD surface errors between the manual reference and proposed method of 2.8 ± 0.4 and 0.2 ± 0.9 mm for the LV, 3.2 ± 0.7 and −0.6 ± 0.9 mm for the RV, and 3.1 ± 0.5 and 0.4 ± 1.0 mm for the LV-EPI. The corresponding HDs were 8.8 ± 3.1 mm for the LV, 14.0 ± 5.5 mm for the RV, and 10.3 ± 2.5 mm for the LV-EPI. A full comparison of surface metrics with respect to the manual references in 3DRTE is shown in Table 2. For the fused LV + RV image, the mean DICE over all frames was 86.4% ± 3.2% for the LV and 77.3% ± 3.9% for the RV.

For the clinical indices, the differences between the proposed volumes and manual measurements in 3DTTE were 7 ± 24 mL EDV, 5 ± 17 mL ESV, −1% ± 5% EF, and −2 ± 27 g mass, for the LV. Similarly, for the RV, they were 7 ± 21 mL EDV, 0 ± 21 mL ESV, and 2% ± 7% EF. For the LV myocardial mass, the differences were −2 ± 27 g. A comprehensive overview of clinical indices is given in Table 3, and Bland–Altman plots of EDV, ESV, and LV mass, compared with the 3DTTE reference, are shown in Figs. 5 and 6. Table 4 shows the interobserver variability of the clinical indices, as measured by the proposed method. Example segmentations are shown in Fig. 7.

6 Discussion

In this work, we developed a geometric representation of coupled basis surfaces, which allows the model to be parameterization by local deformations and local wall volumes. Combined with a Kalman filter state estimation approach, this type of model lends itself to the inclusion of myocardial volume regularization to assist the segmentation. For this to work, it is important that the initial myocardial volume is correct before conservation is applied. This is achieved by performing

Table 3 Results of clinical indices validation.

	Fused images				LV image only		RV image only	
	LV		RV		LV		RV	
Auto versus 3DTTE reference								
EDV (mL)	7.2 ± 24.3	(0.85)	7.3 ± 21.4	(0.91)	8.8 ± 23.0	(0.86)	2.5 ± 21.2	(0.91)
ESV (mL)	5.3 ± 16.9	(0.77)	0.3 ± 20.6	(0.84)	2.1 ± 15.1	(0.83)	-9.0 ± 21.4	(0.80)
SV (mL)	1.9 ± 15.1	(0.80)	7.0 ± 10.0	(0.79)	6.7 ± 18.1	(0.72)	11.5 ± 10.9	(0.67)
EF (%)	-0.7 ± 5.2	(0.51)	2.4 ± 7.2	(0.29)	1.0 ± 5.8	(0.45)	$6.8 \pm 7.8^{*}$	(0.21)
Mass (g)	-1.8 ± 27.1	(0.71)			-1.7 ± 25.3	(0.75)		
Auto versus MRI reference								
EDV (mL)	$-61.5 \pm 23.2^{*}$	(0.52)	-27.9 ± 38.2	(0.67)	$-60.0 \pm 24.0^{*}$	(0.53)	-32.6 ± 38.5	(0.64)
ESV (mL)	$-36.7 \pm 21.3^{*}$	(0.42)	-19.4 ± 33.0	(0.59)	$-40.0 \pm 22.3^{*}$	(0.37)	$-28.7 \pm 32.8^{*}$	(0.53)
SV (mL)	$-24.8 \pm 24.5^{*}$	(0.48)	-8.5 ± 15.6	(0.63)	-20.0 ± 21.2	(0.62)	-3.9 ± 16.8	(0.63)
EF (%)	3.8 ± 8.3	(0.05)	1.2 ± 9.2	(0.31)	$5.5 \pm 8.1^{*}$	(0.13)	5.7 ± 8.7	(0.38)
3DTTE versus MRI reference								
EDV (mL)					$-68.8 \pm 35.8^{*}$	(0.42)	-35.2 ± 32.6	(0.68)
ESV (mL)					$-42.1 \pm 23.4^{*}$	(0.33)	-19.7 ± 26.2	(0.71)
SV (mL)					$-26.7 \pm 30.2^{*}$	(0.39)	$-15.4 \pm 13.4^{*}$	(0.54)
EF (%)					$4.5 \pm 7.5^{*}$	(0.03)	-1.2 ± 6.3	(0.60)

Note: All values are mean $\pm$ SD (ICC).
EDV, end diastolic volume; ESV, end systolic volume; SV, stroke volume; EF, ejection fraction; ICC, intraclass correlation coefficient; LV, left ventricle; RV, right ventricle; EPI, epicardial; END, endocardial.
$^{*}p < 0.05$ by 2-tailed paired Student's t-test.

the state estimation in two passes: first to identify the global pose and myocardial volume and then to capture local shape deformations. For the LV, the method achieved an MAD surface error of 2.8 mm and an HD of 8.8 mm. These measurements are slightly higher than what has been presented by recent state-of-the-art methods, including state-estimation approaches using deformable surfaces,[21] where MAD values of 2.3 mm and HD values of 8.5 mm have been reported.[21,22] One explanation of the higher observed surface errors is the reduced deformational degrees of freedom of the model and the high degree of regularization imposed for a robust biventricular segmentation. Also, misregistration of the LV and RV images, either spatially or temporally, may have introduced uncertainties in the segmentation.

Similarly, the method achieved an MAD error of 3.2 mm and an HD error of 14.0 mm for the RV. An RV segmentation method, using a similar state-estimation approach with a statistical shape model, was recently reported and evaluated on the

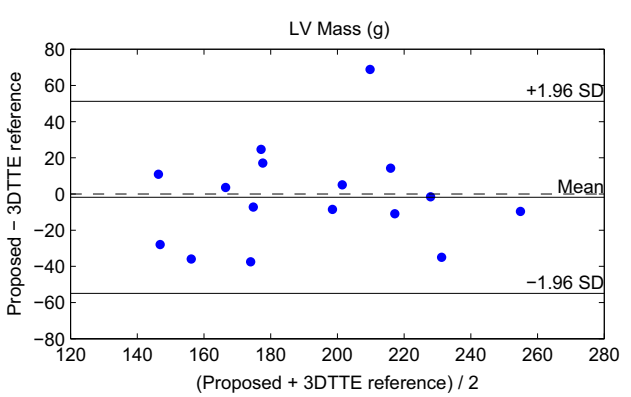

Fig. 6 Comparison of LV myocardial mass, as measured by the proposed method with respect to manual measurements in 3DTTE.

Table 4 Interobserver variation of clinical indices.

	LV		RV	
EDV (mL)	10.1 ± 19.7	(0.90)	-3.3 ± 14.8	(0.96)
ESV (mL)	8.1 ± 12.1	(0.78)	-2.1 ± 9.9	(0.96)
SV (mL)	3.5 ± 8.6	(0.96)	-1.2 ± 8.6	(0.94)
EF (%)	-0.7 ± 3.3	(0.89)	1.0 ± 5.4	(0.84)

Note: All values are mean $\pm$ SD (ICC).
EDV, end diastolic volume; ESV, end systolic volume; SV, stroke volume; EF, ejection fraction; ICC, intraclass correlation coefficient; LV, left ventricle; RV, right ventricle; END, endocardial.

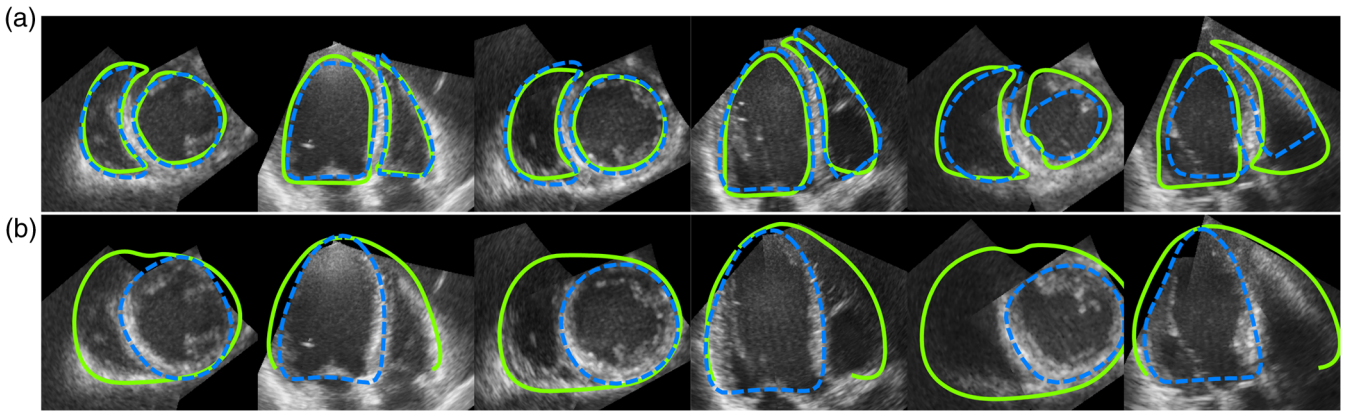

Fig. 7 Example segmentation results, compared to manual references in three cases. Solid green lines show the results of the automated method, and dashed blue lines show the reference contours. (a) endocardial surfaces and (b) epicardial surfaces. Mean absolute surface-errors: 2.8 mm (left), 2.9 mm (center), and 3.9 mm (right, worst case).

same data as the proposed biventricular method, with the exception of an additional case.[12] This method achieved comparable MAD and HD values of 3.6 and 11.6 mm, respectively. A proposed method by Stebbing et al.,[11] which performs RV segmentation simultaneously in multiple images, potentially from multiple patients, achieved median signed trace-surface distances of 1.5 mm (median over 4 cases) for multiple images of a single patient and 1.7 mm (median over 12 cases) for multiple patients. Although these were noticeably lower than what was achieved in our validation (2.5 mm median), the validation methodology was very different.[12]

For the clinical indices, the method achieved good correlation compared to manual measurements in 3DTTE, with clinically acceptable biases in EDV, ESV, SV, and EF for both ventricles, as shown in Table 3 and Fig. 5. However, in a clinical setting, it is likely that manual surface editing must be available to reduce the observed variability and increase confidence in the segmentation. Compared to MRI, we observed an underestimation of EDV, ESV, and SV for both ventricles, although this was only statistically significant for the LV. This underestimation was present for both the reference and automated segmentations and is consistent with what is typically found in the literature, although the observed biases were slightly larger than expected.[23,24] Because of the large differences in measurement methodologies between 3DTTE and MRI, perfect volume correlations should not be expected.[25] For instance, the surfaces in the proposed 3DTTE method are strictly bounded by the valve planes, whereas in MRI, the volume is calculated by short-axis disk summation and, therefore, bounded by a slice approximately in the atrioventricular plane.

Although we applied the surface representation to a two-chamber model, it generalizes trivially to a whole-heart model and to the 2-D case. One limitation with the proposed parameterization, however, is the dependency between the number of control vertices and the number of patch volume states, which makes it hard to perform volume regularization on larger myocardial patches while at the same time increasing the control vertex resolution for higher flexibility in the local deformations. Although a reasonable trade-off was found for the biventricular case, this could be a limiting factor in a four chamber extension. However, using the approach applied in Eq. (15), multiple patches could share a common volume state and thus allow higher resolution deformations with volume conservation of larger myocardial patches.

The computation was efficient, with a mean segmentation time of 2.1 s per recording and 60 ms per frame. This fits well with the interactive nature of echocardiography and is important for any widespread clinical use. The majority of time was spent in sampling the edge profiles, which is an ideal task for parallelization, meaning that significant reduction in time can be made by an implementation utilizing a graphics processing unit.

With the current 3DRTE technology, it is not generally feasible to capture both ventricles in a single ultrasound sector while maintaining sufficient spatial and temporal resolution. Furthermore, the best acoustic windows are typically slightly different for each ventricle. For this reason, we rely on a preprocessing step where two separate 3DRTE sectors are fused to form a single image volume. In this study, the registration was done manually by identifying valvular events and anatomical landmarks, in addition to manual translation and rotation corrections. Misregistration, either due to manual error or nonrigid deformations of the heart in between the LV and RV recordings, could have introduced errors in both the automated and reference segmentations. As the reference segmentations were performed separately for each sector, and in different tools, the fused references were slightly inconsistent, e.g., the septum of the LV-EPI and RV reference surfaces were slightly disjoint, introducing additional uncertainty in the surface error measurements. It is worth noting that methods for automated registration of multiview 3-D ultrasound have been reported with promising results,[26–29] which could eliminate this time-consuming task and potentially increase the registration accuracy, and consequently the segmentation accuracy as well.

One of the challenges associated with RV segmentation in ultrasound is the general lowered image quality and, specifically, the shadowing of the anterior part of the RV outflow tract and anteriolateral free wall due to its position with respect to the sternum and lungs.[30] This issue, along with a larger interpatient variation and increased geometrical complexity compared to the LV, has lead previous works to introduce statistical knowledge of the RV shape and appearance into the segmentation algorithm, either explicitly[12] or implicitly.[11] Although there is nothing preventing the introduction of such information to the

proposed method, e.g., in terms of deformation modes learned from manual segmentations, ultimately this was not included in this work. However, part of the benefits of such a statistical shape model is inherited by the added anatomical information and regularization introduced with the three-surface segmentation approach. Furthermore, we introduce model personalization based on manual identification of key anatomical landmarks, which also reduces the need for such statistical information. Although this approach requires more user interaction, there is no need to perform training on a comprehensive set of images representative of the target population.

7 Conclusion

In this paper, we have presented an automated method for simultaneous segmentation of the endocardial and epicardial borders of both the LV and RV in 3-D real-time echocardiography. The method extends a Kalman filter state estimation framework, previously applied individually to the LV,[5] RV,[12] and aortic root,[19] with a geometrical model of coupled surfaces with wall volume parameterization. The method performed efficiently and achieved good agreement with manual measurements and segmentations in 3-D echocardiography and MRI.

Appendix: Surface Patch Volume

For each patch $\mathcal{P}_{i,j}$ of each surface $\mathcal{S}_i$, the local displacement leaves a volume $v_{i,j}$ between the surface evaluated at $\tilde{\mathbf{Q}}_i(\mathbf{t}_i)$ and $\mathbf{Q}_0$, as shown in Fig. 2(c). In this section, we derive an expression of this volume.

Consider a single surface patch given by

$$\mathbf{p}_0(u,v) = \sum_i \mathbf{q}_i b_i(u,v), \tag{31}$$

for $u, v \in [0,1]$. Displacing each control vertex $\mathbf{q}_i$ by a distance t_i along a unit direction $\mathbf{d}_i$ results in a displaced surface

$$\mathbf{p}_1(u,v) = \sum_i (\mathbf{q}_i + \mathbf{d}_i t_i) b_i(u,v). \tag{32}$$

We seek the volume v that is encapsulated in between the two surface patches.

Each of the surfaces $\mathbf{p}_0$ and $\mathbf{p}_1$ has four edges

$$a: u = 0, \qquad v \in [0,1], \tag{33}$$

$$b: u \in [0,1], \qquad v = 0, \tag{34}$$

$$c: u = 1, \qquad v \in [0,1], \tag{35}$$

$$d: u \in [0,1], \qquad v = 1. \tag{36}$$

Let the two surfaces $\mathbf{p}_0$ and $\mathbf{p}_1$ define the bottom and top faces of a thick "cube" V, as shown in Fig. 8. The remaining faces of V can be parameterized by

$$\mathbf{p}_a(u,v) = u\mathbf{p}_1(0,v) + (1-u)\mathbf{p}_0(0,v), \tag{37}$$

$$\mathbf{p}_b(u,v) = v\mathbf{p}_1(u,0) + (1-v)\mathbf{p}_0(u,0), \tag{38}$$

$$\mathbf{p}_c(u,v) = (1-u)\mathbf{p}_1(1,v) + u\mathbf{p}_0(1,v), \tag{39}$$

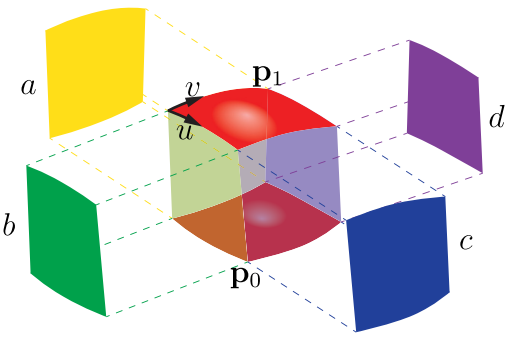

Fig. 8 Illustration of a thick surface patch with bottom side $\mathbf{p}_0(u,v)$, top side $\mathbf{p}_1(u,v)$, and interpolated faces $a-d$ forming a thick "cube."

$$\mathbf{p}_d(u,v) = (1-v)\mathbf{p}_1(u,1) + v\mathbf{p}_0(u,1), \tag{40}$$

for $u, v \in [0,1]$. Using the divergence theorem and the vector field $\mathbf{F} = [0,0,z]$ for which $\nabla \cdot \mathbf{F} \equiv 1$, the volume can be written as

$$v = \iiint_V (\nabla \cdot \mathbf{F}) \mathrm{d}V, \tag{41}$$

$$= \oiint_{(\mathbf{F}\cdot\mathbf{n})\mathrm{d}S}, \tag{42}$$

where S is the surface of V with unit normal $\mathbf{n}$. With the parameterization in Eqs. (37) to (40), this results in

$$\begin{aligned} v = {} & \partial V(\mathbf{p}_1) + \partial V(\mathbf{p}_a) + \partial V(\mathbf{p}_b) + \partial V(\mathbf{p}_c) \\ & + \partial V(\mathbf{p}_d) - \partial V(\mathbf{p}_0), \end{aligned} \tag{43}$$

where

$$\partial V(\mathbf{p}) = \int_0^1 \int_0^1 p_z(u,v) \left(\frac{\partial p_x}{\partial u}\frac{\partial p_y}{\partial v} - \frac{\partial p_y}{\partial u}\frac{\partial p_x}{\partial v} \right) \mathrm{d}u\,\mathrm{d}v. \tag{44}$$

It is useful to separate Eq. (44) into

$$\partial V(\mathbf{p}) = \sum \mathbf{x}^\top \left(\sum_i z_i \mathbf{M}_i \right) \mathbf{y}, \tag{45}$$

where $\mathbf{x}$, $\mathbf{y}$, and $\mathbf{z}$ are the vectors of the x, y, and z coordinates of the control vertices $\mathbf{q}_i$ and

$$\mathbf{M}_i = \int_0^1 \int_0^1 b_i (\mathbf{b}_u \mathbf{b}_v^\top - \mathbf{b}_v \mathbf{b}_u^\top) \mathrm{d}u\,\mathrm{d}v, \tag{46}$$

where $\mathbf{b} = [b_1, \ldots, b_N]^\top$, $\mathbf{b}_u = \frac{\partial \mathbf{b}}{\partial u}$, and $\mathbf{b}_v = \frac{\partial \mathbf{b}}{\partial v}$. With this separation, $\mathbf{M}_i$ is given by the topology of the control mesh and is independent of its vertex positions. This means that Eq. (46) can be evaluated offline with desired numerical accuracy.

Disclosures

Dr. Bersvendsen reports grants from the Research Council of Norway, grants from GE Vingmed Ultrasound, grants from Norwegian Research School in Medical Imaging, and nonfinancial support from the Center for Cardiological Innovation during the conduct of this study. The other authors have nothing to disclose.

References

1. R. M. Lang et al., "EAE/ASE recommendations for image acquisition and display using three-dimensional echocardiography," *J. Am. Soc. Echocardiogr.* **25**(1), 3–46 (2012).
2. M. H. Drazner et al., "Increased left ventricular mass is a risk factor for the development of a depressed left ventricular ejection fraction within five years: the cardiovascular health study," *J. Am. Coll. Cardiol.* **43**(12), 2207–2215 (2004).
3. Y. Zhu et al., "A coupled deformable model for tracking myocardial borders from real-time echocardiography using an incompressibility constraint," *Med. Image Anal.* **14**(3), 429–448 (2010).
4. F. Orderud, G. Kiss, and H. Torp, "Automatic coupled segmentation of endo- and epicardial borders in 3D echocardiography," in *IEEE Ultrasonics Symp. (IUS '08)*, pp. 1749–1752 (2008).
5. F. Orderud and S. I. Rabben, "Real-time 3D segmentation of the left ventricle using deformable subdivision surfaces," in *IEEE Conf. on Computer Vision and Pattern Recognition*, Norwegian University of Science and Technology, IEEE, Trondheim (2008).
6. A. Myronenko, X. Song, and D. J. Sahn, "LV motion tracking from 3D echocardiography using textural and structural information," *Lect. Notes Comput. Sci.* **4792**, 428–435 (2007).
7. V. Tavakoli and A. A. Amini, "A survey of shaped-based registration and segmentation techniques for cardiac images," *Comput. Vision Image Understanding* **117**(9), 966–989 (2013).
8. L. Glass, P. Hunter, and A. McCulloch, Eds., *Theory of Heart: Biomechanics, Biophysics, and Nonlinear Dynamics of Cardiac Function*, Institute for Nonlinear Science, Springer-Verlag, New York (1991).
9. A. Bistoquet, J. Oshinski, and O. Skrinjar, "Left ventricular deformation recovery from cine MRI using an incompressible model," *IEEE Trans. Med. Imaging* **26**, 1136–1153 (2007).
10. E. D. Angelini et al., "Segmentation of real-time three-dimensional ultrasound for quantification of ventricular function: a clinical study on right and left ventricles," *Ultrasound Med. Biol.* **31**, 1143–1158 (2005).
11. R. V. Stebbing et al., "Data-driven shape parameterization for segmentation of the right ventricle from 3D+t echocardiography," *Med. Image Anal.* **21**, 29–39 (2015).
12. J. Bersvendsen et al., "Automated segmentation of the right ventricle in 3D echocardiography: a Kalman filter state estimation approach," *IEEE Trans. Med. Imaging* **35**, 42–51 (2016).
13. D. Doo, "A subdivision algorithm for smoothing down irregularly shaped polyhedrons," in *Proc. on Interactive Techniques in Computer Aided Design*, pp. 157–195, IEEE (1978).
14. E. Catmull and J. Clark, "Recursively generated B-spline surfaces on arbitrary topological meshes," *Comput.-Aided Des.* **10**(6), 350–355 (1978).
15. J. Stam, "Exact evaluation of Catmull–Clark subdivision surfaces at arbitrary parameter values," in *Proc. of the 25th Annual Conf. on Computer Graphics and Interactive Techniques, SIGGRAPH '98*, pp. 395–404, ACM, New York (1998).
16. C. Loop, "Smooth subdivision surfaces based on triangles," Master's Thesis, The University of Utah (1987).
17. J. Stam, *Evaluation of Loop Subdivision Surfaces*, Alias Wavefront, Inc., Seattle, Washington (1998).
18. F. Orderud, "A framework for real-time left ventricular tracking in 3D+T echo, cardiography, using nonlinear deformable contours and Kalman filter based tracking," in *Computers in Cardiology, 2006*, pp. 125–128, Norwegian University of Science and Technology (NTNU), IEEE, Trondheim (2006).
19. J. Bersvendsen et al., "Automatic measurement of aortic annulus diameter in 3-dimensional transoesophageal echocardiography," *BMC Med. Imaging* **14**, 13 (2014).
20. D. Fraser and J. Potter, "The optimum linear smoother as a combination of two optimum linear filters," *IEEE Trans. Autom. Control* **14**, 387–390 (1969).
21. E. Smistad and F. Lindseth, "Real-time tracking of the left ventricle in 3D ultrasound using Kalman filter and mean value coordinates," *MIDAS J.* (2014).
22. D. Barbosa et al., "Fast tracking of the left ventricle using global anatomical affine optical flow and local recursive block matching," *MIDAS J.* (2014).
23. Y. J. Shimada et al., "Accuracy of right ventricular volumes and function determined by three-dimensional echocardiography in comparison with magnetic resonance imaging: a meta-analysis study," *J. Am. Soc. Echocardiogr.* **23**, 943–953 (2010).
24. J. L. Dorosz et al., "Performance of 3-dimensional echocardiography in measuring left ventricular volumes and ejection fraction systematic review and meta-analysis," *J. Am. Coll. Cardiol.* **59**(20), 1799–1808 (2012).
25. G. Leibundgut et al., "Dynamic assessment of right ventricular volumes and function by real-time three-dimensional echocardiography: a comparison study with magnetic resonance imaging in 100 adult patients," *J. Am. Soc. Echocardiogr.* **23**, 116–126 (2010).
26. V. Grau, H. Becher, and J. Noble, "Registration of multiview real-time 3-D echocardiographic sequences," *IEEE Trans. Med. Imaging* **26**, 1154–1165 (2007).
27. D. Ni et al., "Volumetric ultrasound panorama based on 3D sift," *Lect. Notes Comput. Sci.* **5242**, 52–60 (2008).
28. K. Rajpoot et al., "Multiview RT3D echocardiography image fusion," *Lect. Notes Comput. Sci.* **5528**, 134–143 (2009).
29. J. Bersvendsen et al., "Robust spatio-temporal registration of 4D cardiac ultrasound sequences," *Proc. SPIE* **9790**, 97900F (2016).
30. E. Ostenfeld et al., "Manual correction of semi-automatic three-dimensional echocardiography is needed for right ventricular assessment in adults; validation with cardiac magnetic resonance," *Cardiovasc. Ultrasound* **10**, 1 (2012).

Biographies for the authors are not available.